# Graphite Conjugated Nickel Phthalocyanine for Efficient $CO_2$ Electroreduction and Zn-$CO_2$ Batteries

Jingwei Han,[†] Qiang Xu,[†] Fengkun Tian,[†] Hai Sun,[†] Yuanyuan Qi,[†] Guodong Zhang,[§] Jun-Sheng Qin,[†] Heng Rao[†*]

[†]State Key Laboratory of Inorganic Synthesis and Preparative Chemistry, College of Chemistry, International Center of Future Science, Jilin University, 2699 Qianjin Street, Changchun 130012, P. R. China

[§]School of Chemistry and Chemical Engineering, Yangzhou University, Siwangting Road 180, Yangzhou, P. R. China

*Correspondence to: rao@jlu.edu.cn

## Table of contents

## Chemical and materials

4-Nitrophthalic acid ($C_8H_5NO_6$, 98%), ammonium molybdate ($(NH_4)_2MoO_4$, 98%), and urea ($CO(NH_2)_2$, 99%) were purchased from Aladdin. 2,3,9,10,16,17,23,24-Octaaminophthalocyanine nickel (II) ($Ni(NH_2)_8Pc$) and Tetraaminophthalocyaninato nickel (II) ($Ni(NH_2)_4Pc$) were purchased from Yanshen Technology Co., Ltd. Monarch 1300 was obtained from Cabot. Toluene (MePh, AR), nickel chloride hexahydrate ($NiCl_2•6H_2O$, 99%), potassium hydrogen carbonate ($KHCO_3$, 99%), thionyl chloride ($SOCl_2$, AR), and dimethyl sulfoxide (DMSO, AR) were purchased from Beijing InnoChem Science & Technology Co., Ltd. Potassium hydroxide (KOH, 95%), sodium chloride (NaCl, AR), sodium hydroxide (NaOH, AR), and zinc acetate ($Zn(CH_3COO)_2$, 99%) were purchased from Macklin. Ammonium chloride ($NH_4Cl$, AR), hydrochloric acid (HCl, 36%), and nitric acid ($HNO_3$, 69%) were obtained from Sinopharm Chemical Reagent Co., Ltd. All electrodes were obtained from Gaoss Union (Tianjin). All chemicals were used as received, and all aqueous electrolyte solutions were prepared with reagent-grade water (18.2 MΩ cm) unless otherwise stated.

## Preparation of -COCl modified GC

Monarch 1300 carbon powder (200 mg) and dry toluene (100 mL) were added to a flask. Against positive pressure of Ar, $SOCl_2$ (50 mL) was injected into the flask slowly. Then, the mixture was refluxed at 120 °C for 2 hours under argon atmosphere. Following cooling, the excess $SOCl_2$ was removed by rotary evaporation. Then, the solid was rinsed with copious amounts of toluene and $CH_3COOH$ and dried in a vacuum.

## Preparation of $Ni(NH_2)_8Pc$-GC

Monarch 1300 carbon powder (125 mg) was ultrasonically dispersed in EtOH (9 mL) for 30 minutes, followed by sparging with Ar for 30 minutes to remove oxygen. Under the protection of Ar, a solution of $Ni(NH_2)_8Pc$ (12.5 mg) in DMSO (10 mL) was added by injection, and the mixture was heated to 130 °C for 24 hours. To remove unsupported $Ni(NH_2)_8Pc$, after cooling to room temperature, the powder was collected by centrifugation and washed with DMSO and EtOH several times. The powder was subsequently treated with 0.1 M HCl for 4 hours to hydrolyze imine bonds formed on the surface. Following the acid soak, the powder was collected by centrifugation and washed with water 5 times and EtOH thrice. Finally, the product dried at room temperature under vacuum overnight.

**Preparation of $Ni(NH_2)_4Pc$-GC**

Following the same procedures, $Ni(NH_2)_4Pc$-GC was prepared by replacing the $Ni(NH_2)_8Pc$ and Monarch 1300 with $Ni(NH_2)_4Pc$ and Monarch 1300-COCl, respectively.

**Preparation of $Ni(NH_2)_8Pc$/GC**

Monarch 1300 carbon powder (9.1 mg) was ultrasonically dispersed in isopropanol (1 mL) for 30 minutes to form ink I. $Ni(NH_2)_8Pc$ (2.0 mg) was dissolved in DMSO (2 mL) to form ink II. Ink I (1 mL) was mixed with ink II (900 μL) and further sonicated for 30 minutes to form ink III.

**Preparation of $Ni(NH_2)_4Pc$/GC**

Following the same procedures, $Ni(NH_2)_4Pc$/GC was prepared by replacing the $Ni(NH_2)_8Pc$ and Monarch 1300 with $Ni(NH_2)_4Pc$ and Monarch 1300-COCl, respectively.

**Characterization**

X-ray diffraction (XRD) patterns were obtained by a Rigaku D/Max2550 with Cu Kα (λ=1.5418 Å). Raman spectra were conducted on a Jobin Yvon/HORIBA LabRam ARAMIS Raman spectrometer with an excitation of 532 nm laser light. The morphology and element distribution of the catalysts were studied by scanning electron microscopy (SEM, JSM-6510) and transmission electron microscopy (TEM, Philips-FEI Tecnai G 2S-Twin F20) equipped with energy dispersive X-ray spectroscopy (EDX). The composition and chemical states of elements on the surface of materials were characterized by X-ray photoelectron spectroscopy (XPS, Thermo Electron Corporation ESCALAB 250 spectrometer) equipped with Al Kα. UV-vis spectra were recorded on Ocean Insight QE65Pro High-Sensitivity spectrometer. Brunauer-Emmett-Taller (BET) specific surface area and pore size distribution were calculated based on $N_2$ adsorption/disadsorption isotherms recorded on a Micromeritics ASAP 3-flex. The concentrations of Ni in the catalysts were quantitatively analyzed by inductively coupled plasma optical emission spectroscopy (ICP-OES, Perkin-Elmer Optima 3300 DV). Gases from headspace during electrolysis were performed on a Shimadzu GC-2014 gas chromatography (GC) system equipped with a thermal conductivity detector (TCD) and a flame ionization detector (FID).

The attenuated total reflectance surface-enhanced infrared spectroscopy (ATR-SEIRAS)

was performed on Bruker vertex 80v machine with a mercury cadmium telluride (MCT) detector. All spectra were acquired at 4 $cm^{-1}$ spectral resolution and 32 scans. The electrolytic cell consists of a polytetrafluoroethylene pedestal and a glass reactor. $CO_2$-saturated 0.5 M $KHCO_3$ solution was used as the electrolyte, and $CO_2$ was continuously fed into the electrolyte during the test. The catalyst ink was evenly dropped on the germanium crystal coated with gold film and used as the working electrode. Ag/AgCl and the Pt wire were used as the reference electrode and the counter electrode, respectively. The background spectrum was collected at open circuit potential. The potential was set from -0.18 V to -0.98 V *vs.* RHE, and the spectra were collected every 100 mV.

**$CO_2$RR in the H-Cell**

All electrochemical measurements were conducted at room temperature on a CH instrument (model CHI 660E Analyzer). The $CO_2$RR was tested in an H-type cell separated by a proton-exchange membrane (Nafion-117). The catalyst-coating carbon paper, platinum foil and Ag/AgCl (in saturated KCl electrolyte) were employed as working electrode, counter electrode and reference electrode, respectively. 0.5 M $KHCO_3$ was used as an electrolyte. 5 mg of prepared catalysts and 50 μL of Nafion (5 wt%) were dispersed into 1 mL isopropanol/water mixture (v : v = 7 : 3) by 30 minutes sonication to form a homogenous suspension. A certain amount of ink was drop-coated on carbon paper (Y30T, 1 × 1 $cm^2$) with a catalyst loading of 0.5 mg $cm^{-2}$. Electrode potentials for experiments conducted in aqueous media were plotted *vs.* the reversible hydrogen electrode (RHE, $E_{RHE}=E_{Ag/AgCl}$ + 0.198 + pH × 0.059 V). All glass instruments were soaked in aqua regia for at least 30 minutes and rinsed with water before use. The linear sweep voltammetry (LSV) was tested in Ar-saturated or $CO_2$-saturated electrolytes with 80% iR compensation at a scan rate of 5 mV $s^{-1}$. During controlled potential electrolysis at different applied potentials, the cathode chamber rotor was stirred at a constant speed of 500 rpm.

**$CO_2$RR in the Flow Cell**

The flow cell performances were tested on a CorrTest CS Studio electrochemical workstation at room temperature. The flow cell purchased from Gaoss Union consists of an anodic chamber, a cathodic chamber, a gas chamber and gaskets, wherein the anodic chamber and cathodic chamber were separated by an anion-exchange membrane (fumasep FAB-PK-130). A microporous gas diffusion layer (GDL, Y30T, 1.5 × 3.5 $cm^2$) with the catalyst loading

of 0.5 mg $cm^{-2}$ was employed as the working electrode, and its actual working area is 0.5 × 2 $cm^2$. A platinum foil (1.5 × 3.5 $cm^2$) and Hg/HgO (with 1 M KOH) were used as counter electrode and reference electrode, respectively. 1 M KOH (pH = 13.6) was used as electrolyte both anolyte and catholyte. The flow rate of electrolyte was set at 2.5 mL $min^{-1}$ by controlling a peristaltic pump. High-purity $CO_2$ (99.999%) from the back side and through the GDE to the catalyst surface at a flow rate of 20 sccm. The potentials were converted to RHE without iR compensations by the following equation: $E_{RHE}=E_{Hg/HgO} + 0.98 + pH \times 0.059$ V.

**Zn-$CO_2$ battery measurements**

The performance of an aqueous rechargeable Zn-$CO_2$ battery was measured in a two-compartment cell equipped with a bipolar membrane (Fumasep FBM-PK). A 1 × 1 $cm^2$ hydrophobic carbon paper with a catalyst loading of 0.5 mg $cm^{-2}$ and a polished 2 × 5 $cm^2$ Zn foil was used as the cathode and anode, respectively. 0.8 M $KHCO_3$ acted as a catholyte, and 6 M KOH with 0.2 M $Zn(Ac)_2$ mixture acted as an anolyte. Throughout the test process, $CO_2$ was continuously pumped into the catholyte at a rate of 20 sccm. All electrochemical measurements were tested on a CHI 660E electrochemical workstation.

The theoretical potential of the Zn-$CO_2$ battery was calculated based on Zhang's work.[1] When the aqueous Zn-$CO_2$ battery is discharged, the reactions that may occur are as follows:

**Cathode:**

$$CO_2 + 2H^+ + 2e^- \rightarrow CO + H_2O \ (0.8\ M\ KHCO_3\ sat.\ CO_2, pH = 7.2)$$

$$E_c = E^{\theta}_{CO_2/CO} - \frac{RT}{nF} ln\left[\frac{1}{\alpha^{\ 2}_{H^+}}\right] = -0.106\ V - \frac{8.314 \times 298.15}{2 \times 96485} ln\left[\frac{1}{(10^{-7.2})^2}\right] V = -0.532\ V$$

Where

$$E^{\theta}_{CO_2/CO} = -0.106\ V\ vs.\ SHE$$

**Anode:**

$$Zn - 2e^- \rightarrow Zn^{2+} \ (6\ M\ KOH\ with\ 0.2\ M\ Zn(CH_3COO)_2)$$

$Zn^{2+}$ will react spontaneously with $OH^-$:

$$Zn^{2+} + 4OH^- \rightarrow Zn(OH)^{2-}_4$$

When Zn(OH)2- 4 is supersaturated:

$$Zn(OH)^{2-}_4 \rightarrow 2OH^- + ZnO + H_2O$$

$$E_a = E^{\theta}_{Zn(OH)^{2-}_4/Zn} - \frac{RT}{nF} ln\left[\frac{\alpha_{Zn} \times \alpha^{\ 4}_{OH^-}}{\alpha_{Zn(OH)^{2-}_4}}\right] = -1.199\ V - \frac{8.314 \times 298.15}{2 \times 96485} ln\left[\frac{6^4}{0.2}\right] V = -1.312\ V$$

Where

$E^{\theta}_{Zn(OH)^{2-}_4/Zn} = -1.199\ V\ vs.\ SHE$

Overall discharge reaction:

$Zn + CO_2 + 2H^+ + 4OH^- \rightarrow Zn(OH)^{2-}_4 + CO + H_2O$

$E_{discharge} = E_c - E_a = -0.532\ V - (-1.312\ V) = 0.78\ V$

$E_c^{'} = E^{\theta}_{H^+/H_2} - \frac{RT}{nF} ln\left[\frac{1}{\alpha^{2}_{H^+}}\right] = 0\ V - \frac{8.314 \times 298.15}{2 \times 96485} ln\left[\frac{1}{(10^{-7.2})^2}\right] V = -0.425\ V$

Where

$E^{\theta}_{H^+/H_2} = 0\ V\ vs.\ SHE$

$E_{discharge}^{'} = E_c^{'} - E_a = -0.425\ V - (-1.312\ V) = 0.887\ V$

When the aqueous Zn-$CO_2$ battery is charged, the reactions that may occur are as follows:

**Cathode:**

$H_2O \rightarrow \frac{1}{2}O_2 + 2H^+ + 2e^-$

$E_c = E^{\theta}_{H_2O/O_2} - \frac{RT}{nF} ln\left[\frac{1}{\alpha^{2}_{H^+}}\right] = 1.229\ V - \frac{8.314 \times 298.15}{2 \times 96485} ln\left[\frac{1}{(10^{-7.2})^2}\right] V = 0.803\ V$

Where

$E^{\theta}_{H_2O/O_2} = 1.229\ V\ vs.\ SHE$

**Anode:**

$Zn(OH)^{2-}_4 \rightarrow 4OH^- + Zn^{2+}$

$Zn^{2+} + 2e^- \rightarrow Zn$

When Zn(OH)2- 4 is undersaturated:

$2OH^- + ZnO + H_2O \rightarrow Zn(OH)^{2-}_4$

This reaction is the inverse of the discharge process, thus $E_a$= -1.312 V

Overall charge reaction:

$Zn(OH)^{2-}_4 + H_2O \rightarrow Zn + \frac{1}{2}O_2 + 2H^+ + 4OH^-$

$E_{charge} = E_c - E_a = 0.803\ V - (-1.312\ V) = 2.115\ V$

The overall reaction of aqueous rechargeable Zn-$CO_2$ battery is summarized as follows:

$CO_2 \rightarrow CO + \frac{1}{2}O_2$

**Determination of Ni surface concentration in $Ni(NH_2)_8$Pc-GC**

Cyclic voltammetry of $Ni(NH_2)_8Pc$-GC modified carbon paper was collected in 0.5 M $KHCO_3$ under Ar. The carbon paper substrate was treated with acid to eliminate residual metal ions prior to its application. The loading amount of $Ni(NH_2)_8Pc$-GC on the surface of the carbon paper electrode is 0.5 mg $cm^{-2}$. The voltammogram was started at the open circuit potential (OCP) and swept negatively, cycling between -0.48 V and 0.92 V vs RHE with a scan rate of 10 mV $s^{-1}$. The redox waves centered at 0.15 V *vs.* RHE were attributed to pyrazine linkages and were integrated to calculate the charge that passed in the pyrazine wave.

By integrating the oxidation and reduction peaks, the corresponding peak areas (S) are found to be $2.9 \times 10^{-5}$ V·A and $3.1 \times 10^{-5}$ V·A, respectively (**Figure 1d**). The integrated charge of the pyrazine wave of $Ni(NH_2)_8Pc$-GC was determined by the following equations:

$$Q_{ox} = \frac{S_{ox}}{\upsilon}$$

$$Q_{red} = \frac{S_{red}}{\upsilon}$$

$$Q_{pyr} = \frac{Q_{ox} + Q_{red}}{2}$$

$S_{ox}$ is the area of the oxidation peak ($2.9 \times 10^{-5}$ V·A).

$S_{red}$ is the area of the reduction peak ($3.1 \times 10^{-5}$ V·A).

υ is the scan rate when performing CV testing (10 mV $s^{-1}$)

$Q_{ox}$ is the charge that passed in the oxidation peak of pyrazine group (C).

$Q_{red}$ is the charge that passed in the reduction peak of pyrazine group (C).

$Q_{pyr}$ is the charge that passed in the pyrazine wave (C).

According to the above formula, we determine that the integrated charge of the pyrazine wave is $3.0 \times 10^{-3}$ C.

Following cyclic voltammetry, the electrode was soaked in ca. 2 mL aqua regia overnight, and the solution was eventually diluted to 50 mL with water. The concentration of Ni in solution was determined by ICP-OES. The results indicate that the Ni content in $Ni(NH_2)_8Pc$-GC was 0.1562 wt%. The number of electrons transferred during the electrochemical reaction at each Ni site were determined using the following equation:

$$Q_{pyr} = n \times (e^- / Ni) \times F$$

n is the molar mass of Ni supported on the surface of the carbon paper (mol).

$e^-$/Ni is the umber of electrons transferred at each Ni site.

F is Faraday's constant (96485 C $mol^{-1}$).

The above formula also was expressed as:

$$3.0 \times 10^{-3}\, C = \frac{0.5 \times 10^{-3}\, g \times 0.1562\, wt\%}{58.6934\, g\, mol^{-1}} \times \left(\frac{e^-}{Ni}\right) \times 96485\, C\, mol^{-1}$$

According to above equation, the $e^-$/Ni ratio of 2.3 was obtained.

The area-normalized content of $Ni(NH_2)_8Pc$ in $Ni(NH_2)_8Pc$-GC electrode was determined by the following equation:

$$\Gamma_{Ni} = \frac{Q_{pyr}}{R_{e^-/Ni} F A}$$

$\Gamma_{Ni}$ is the concentration of nickel (mol $cm^{-2}$).

$Q_{pyr}$ is the charge that passed in the pyrazine wave (C).

$R_{e^-/Ni}$ is the ratio of electrons to nickel rounded to the nearest integer.

A is the geometric area of carbon paper (1 $cm^2$).

**Determination of Ni surface concentration in $Ni(NH_2)_4Pc$-GC**

The content of $Ni(NH_2)_4Pc$ in $Ni(NH_2)_4Pc$-GC electrode was determined by ICP-OES and the following equation:

$$\Gamma_{Ni} = \frac{m_{Ni}}{M_{Ni} \times A} = \frac{0.5 \times 10^{-3}\, g \times 0.466\, wt\%}{58.6934\, g\, mol^{-1} \times 1\, cm^2} = 3.97 \times 10^{-8}\, mol\, cm^{-2}$$

$m_{Ni}$ is the mass of Ni supported on the surface of the carbon paper (g).

$M_{Ni}$ is the ratio of electrons to nickel rounded to the nearest integer (58.6934 g $mol^{-1}$).

**Calculation of Faradic efficiency (FE)**

In H-Cell:

$$FE_g = \frac{Q_g}{Q_{total}} \times 100\% = \frac{\frac{V_g}{V_m} \times N \times F \times 100\%}{Q_{total}}$$

In Flow-Cell:

$$FE_g = \frac{j_g}{j_{total}} \times 100\% = \frac{F \times N \times x_g \times v_{CO_2} \times 100\%}{j_{total}}$$

$V_g$ is the volume of CO or $H_2$ above the cathode chamber (L).

$V_m$ is the molar volume of gases at 25 °C (L $mol^{-1}$).

N is the number of electrons transferred to produce a molecule of CO or $H_2$ ($2e^-$).

F is Faraday's constant (96485 C $mol^{-1}$).

$Q_{total}$ is the charge consumed during electrolysis (C).

$x_g$ is the concentration of CO or $H_2$ measured by GC (mol $mol^{-1}$).

$v_{CO_2}$ is the flow rate of $CO_2$ (mol $s^{-1}$).

$j_{total}$ is the recorded current density (A $cm^{-2}$).

**Calculation of Turnover frequency (TOF)**

The turnover frequency ($s^{-1}$) for CO was calculated as follows:

$$TOF = \frac{j_{total} \times FE_{CO}}{2F \times \Gamma_{Ni}}$$

$j_{total}$ is the recorded current density (A $cm^{-2}$).

$FE_{CO}$ is the faradic efficiency of CO.

F is Faraday's constant (96485 C $mol^{-1}$).

$\Gamma_{Ni}$ is the concentration of nickel (mol $cm^{-2}$).

**Calculation of energy efficiency (EE)**

The half-cell energy efficiency of CO was calculated by the following equation:

$$EE = \frac{1.23 - E_{CO}}{1.23 - E_{applied}} \times FE_{CO} \times 100\%$$

$E_{CO}$ is the thermodynamic potential for the reduction of $CO_2$ to CO ($E_{CO}$ = -0.11 V *vs.* RHE).

$E_{applied}$ is the applied potential *vs.* RHE.

$FE_{CO}$ is the faradic efficiency of CO.

**Calculation of the single-pass $CO_2$-to-CO conversation (SPCC)**

$$SPCC = \frac{\varphi_{CO} \times v_{CO_2}}{v_{CO_2}}$$

Φco is the volume fraction in the gas mixture analyzed.

$v_{CO_2}$ is the flow rate of $CO_2$ (mL $min^{-1}$).

**Calculation of the CO yield rate ($YR_{CO}$)**

$$YR_{CO} = \frac{\varphi_{CO} \times v_{CO_2}}{A}$$

Φco is the volume fraction in the gas mixture analyzed.

$v_{CO_2}$ is the flow rate of $CO_2$ (mL $min^{-1}$).

A is the geometric area of carbon paper (1 $cm^2$).

**Density functional theory (DFT) calculations**

All calculations were implemented in Materials Studio with the DMol3 code. The Perdew–Burke–Ernzerhof (PBE) functional of the generalized gradient approximation (GGA) was used to calculate the exchange–correlation energy. The double numerical plus polarization (DNP) was chosen during the geometry optimization. The convergence tolerances of energy change, maximum force, and maximum displacement were set as $2 \times 10^{-5}$ Ha, 0.004 Ha/Å, and 0.005 Å, respectively.

The Gibbs free energy change is defined as:

$$\Delta G = \Delta E + \Delta ZPE - T\Delta S$$

where $\Delta E$ is the electronic energy calculated with VASP, $\Delta ZPE$ and $\Delta S$ are the zero-point energy difference and the entropy change between the products and reactants, respectively, and T is the temperature (298.15 K).

The elementary steps on the catalysts were:

$$* + CO_2 + H^+ + e^- \rightarrow *COOH$$

$$*COOH + H^+ + e^- \rightarrow *CO + H_2O$$

$$*CO \rightarrow * + CO$$

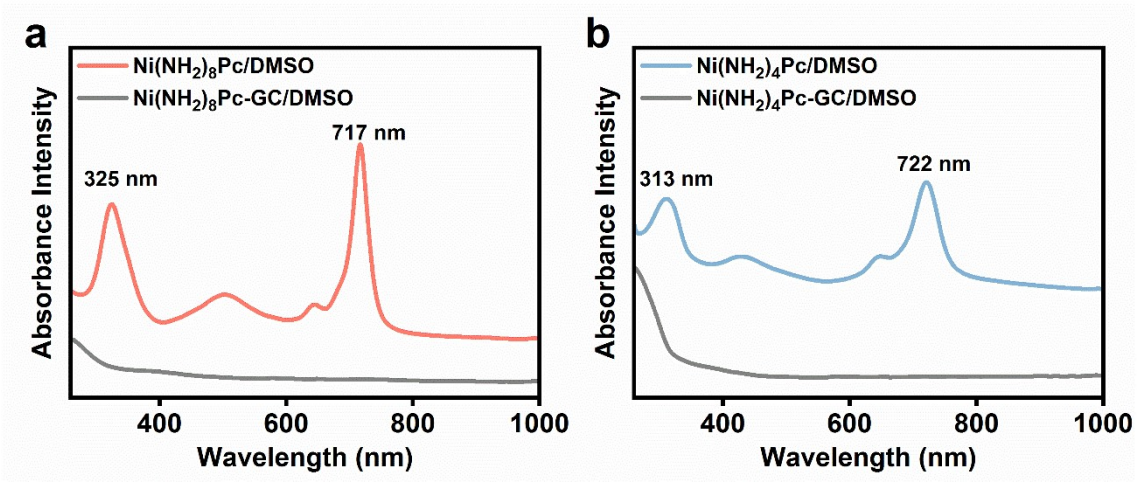


**Figure S1.** UV-visible spectra. (a) $Ni(NH_2)_8Pc$ and filtrate of $Ni(NH_2)_8Pc$-GC washed with DMSO. (b) $Ni(NH_2)_4Pc$ and filtrate of $Ni(NH_2)_4Pc$-GC washed with DMSO.

In general, the UV-visible spectra of phthalocyanines exhibit a distinct sharp Q-band within the range of 600–800 nm. Additionally, a characteristic B-band is observed at 300–400 nm. The pronounced Q-band arises from the π-π* transition between the ground state (HOMO) and the excited state (LUMO). The B-band is attributed to the transition between $a_{2u}$ or $b_{2u}$ and eg orbitals. The presence of additional amino substituents in $Ni(NH_2)_8Pc$ enhances the electron cloud density of the nitrogen atoms within the molecule. The reduction in the energy level difference of the electronic transition ultimately results in a blue shift of the Q-band. Furthermore, the absence of the Q-band of nickel phthalocyanine in the UV-visible spectra of the graphite carbon catalyst indicates the effective removal of the physically adsorbed active sites.

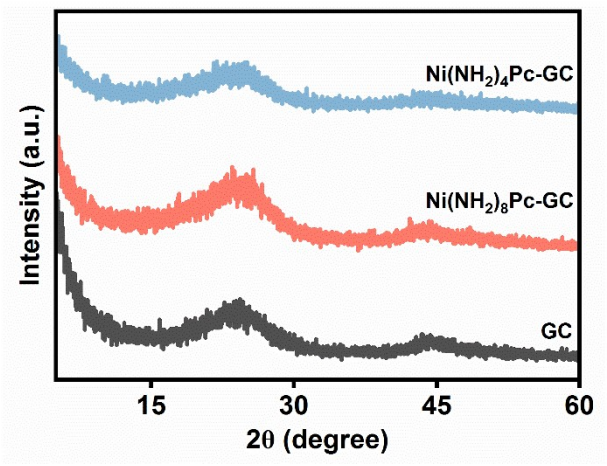


**Figure S2.** XRD patterns of GC, $Ni(NH_2)_8Pc$-GC and $Ni(NH_2)_4Pc$-GC.

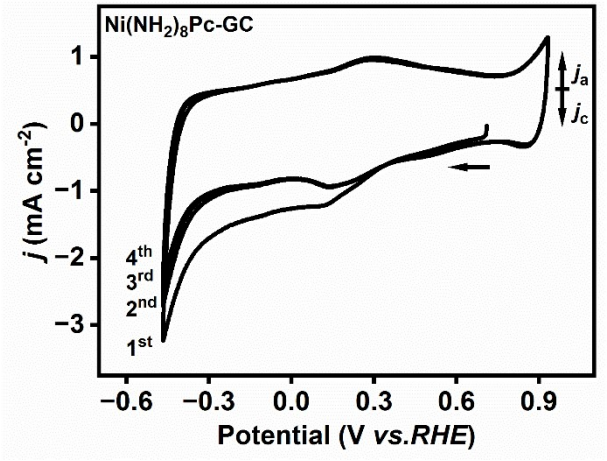


**Figure S3.** Representative CVs of $Ni(NH_2)_8Pc$-GC in Ar-saturated 0.5 M $KHCO_3$ solution with a scan rate of 5 mV $s^{-1}$.

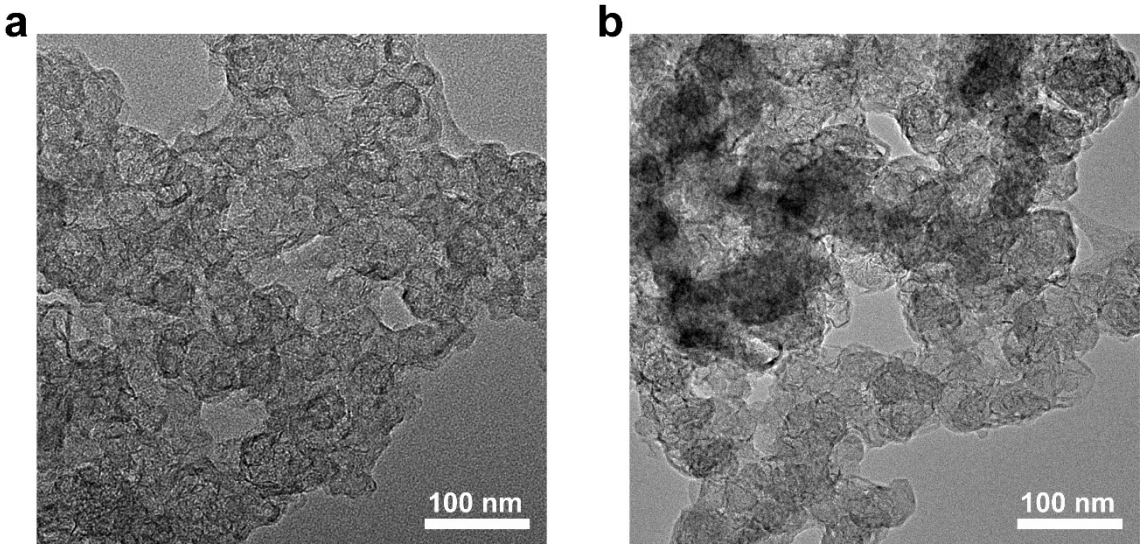


**Figure S4.** TEM images of freshly prepared catalysts. (a) $Ni(NH_2)_8Pc$-GC. (b) $Ni(NH_2)_4Pc$-GC.

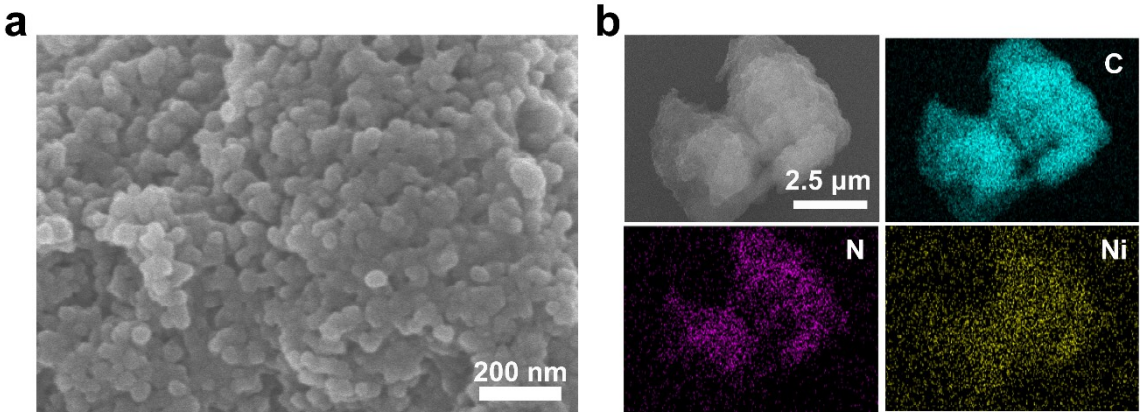


**Figure S5.** SEM image and Elemental mapping of $Ni(NH_2)_8Pc$-GC.

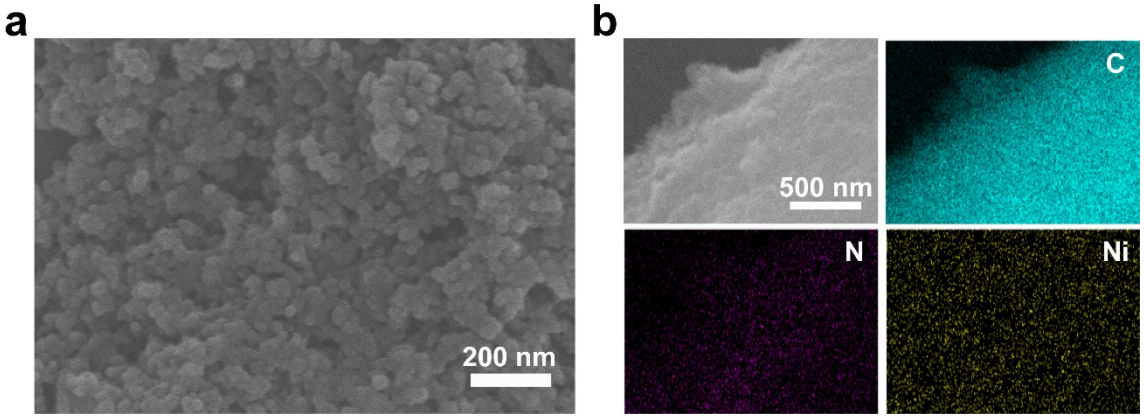


**Figure S6.** SEM image and Elemental mapping of $Ni(NH_2)_4Pc$-GC.

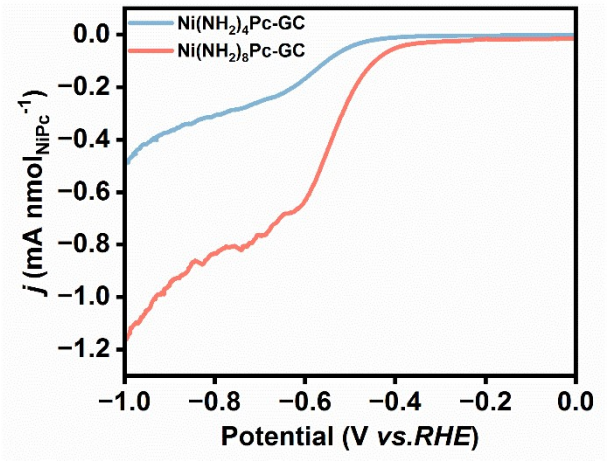


**Figure S7.** LSV curves normalized to the amount of substance of the NiPc species in $CO_2$-saturated 0.5 M $KHCO_3$ solution with a scan rate of 5 mV $s^{-1}$ and 80% iR compensation.

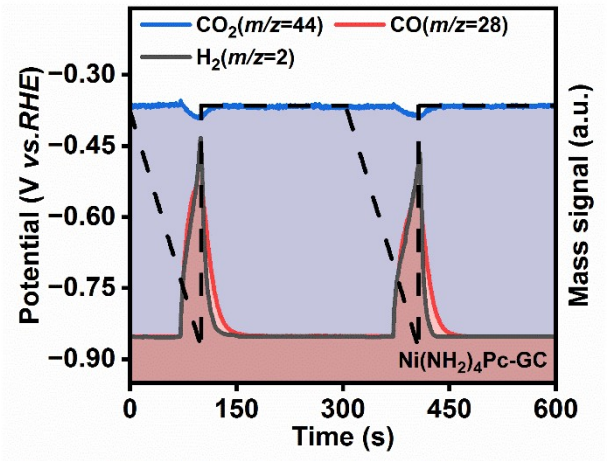


**Figure S8.** In situ DEMS spectrum of $Ni(NH_2)_4Pc$-GC in a $CO_2$-saturated 0.5 M $KHCO_3$ electrolyte. The signals of $CO_2$ (*m/z*=44), CO (*m/z*=28) and $H_2$ (*m/z*=2) were captured twice of LSV from -0.38 to -0.88 V *vs.* RHE. The dashed line represents the potential profile.

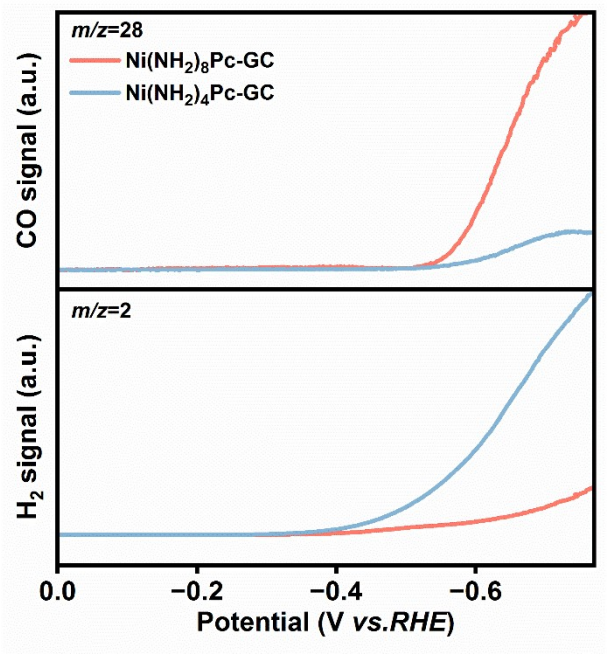


**Figure S9.** In situ DEMS spectra of CO (top, *m/z*=28) and $H_2$ (bottom, *m/z*=2) on $Ni(NH_2)_8Pc$-GC and $Ni(NH_2)_4Pc$-GC in a $CO_2$ saturated 0.5 M $KHCO_3$ electrolyte.

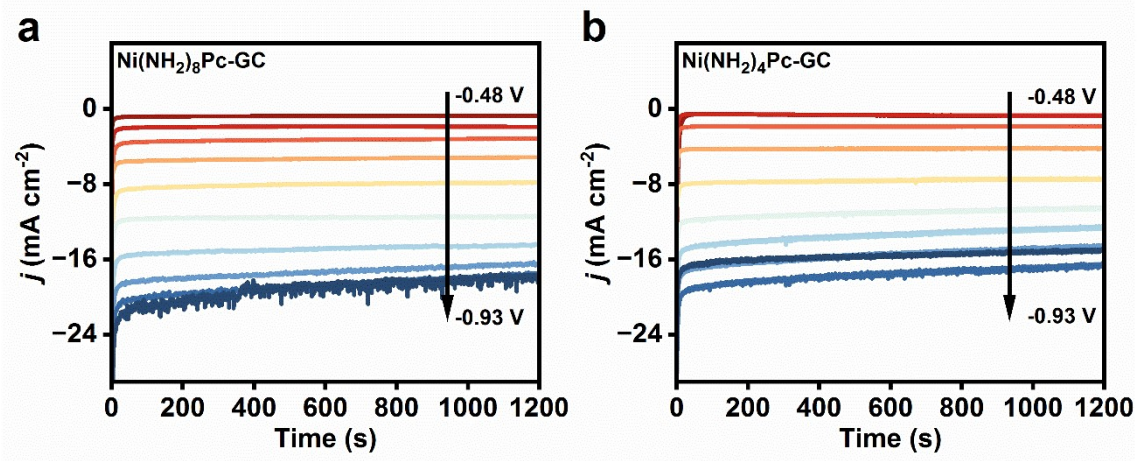


**Figure S10.** Chronoamperometry curves at different potential for $CO_2RR$ of catalysts. (a) $Ni(NH_2)_8Pc$-GC. (b) $Ni(NH_2)_4Pc$-GC.

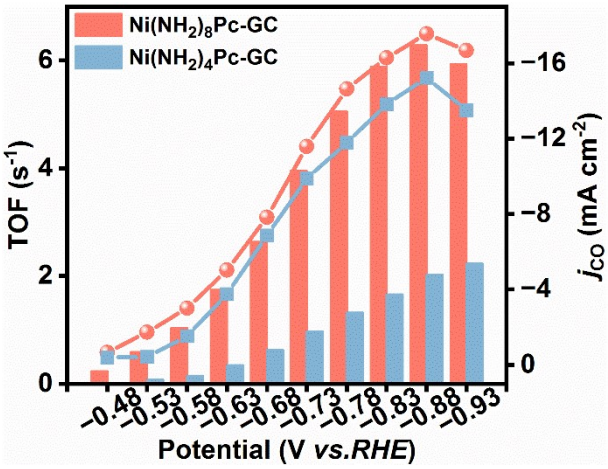


**Figure S11.** Partial current densities and TOF of CO at different applied potentials of $Ni(NH_2)_8Pc$-GC and $Ni(NH_2)_4Pc$-GC.

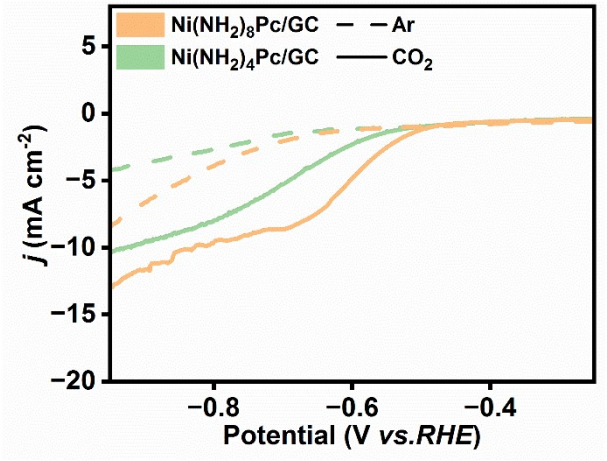


**Figure S12.** LSV curves of $Ni(NH_2)_8Pc$/GC and $Ni(NH_2)_4Pc$/GC in Ar or $CO_2$-saturated 0.5 M $KHCO_3$ solution with a scan rate of 5 mV $s^{-1}$ and 80% iR compensation (Rs=7.1 Ω).

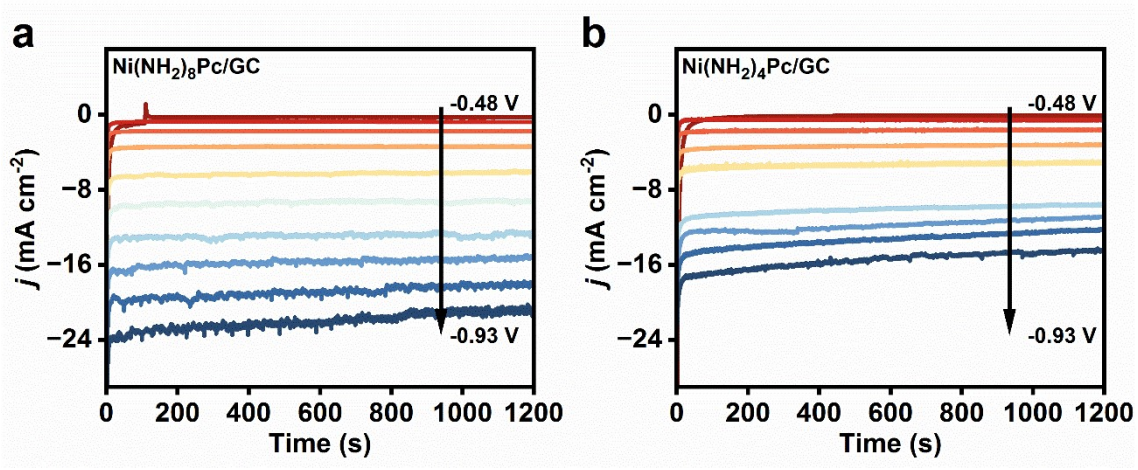


**Figure S13.** Chronoamperometry curves at different potential for $CO_2$RR of catalysts. (a) $Ni(NH_2)_8Pc$/GC. (b) $Ni(NH_2)_4Pc$/GC.

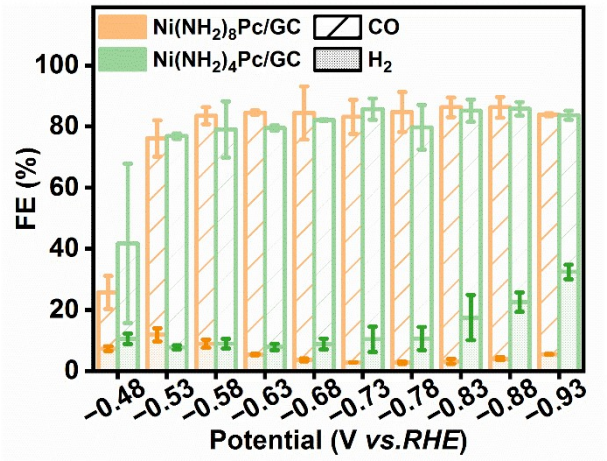


**Figure S14.** FEs of $Ni(NH_2)_8Pc$/GC and $Ni(NH_2)_4Pc$/GC at different applied potentials (three measurements at each potential).

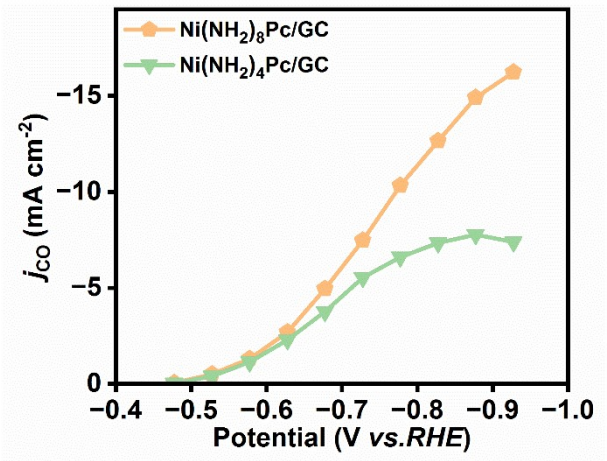


**Figure S15.** CO partial current density of $Ni(NH_2)_8Pc$/GC and $Ni(NH_2)_4Pc$/GC at different applied potentials.

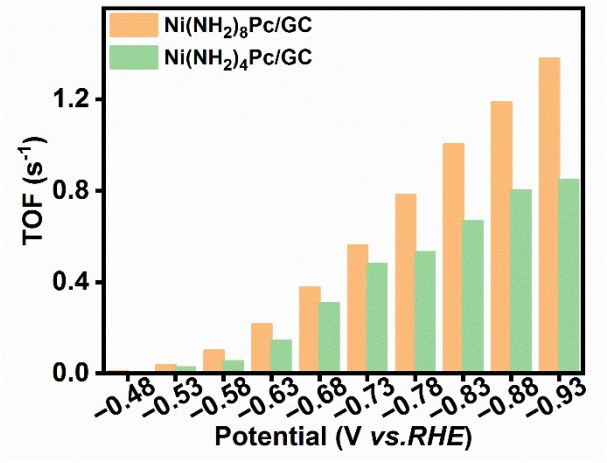


**Figure S16.** TOF of $Ni(NH_2)_8Pc$/GC and $Ni(NH_2)_4Pc$/GC at different applied potentials.

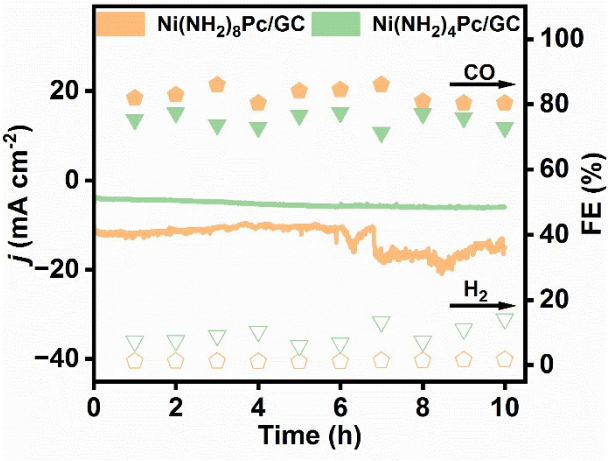


**Figure S17.** Long-term stability tests of $Ni(NH_2)_8Pc$/GC and $Ni(NH_2)_4Pc$/GC.

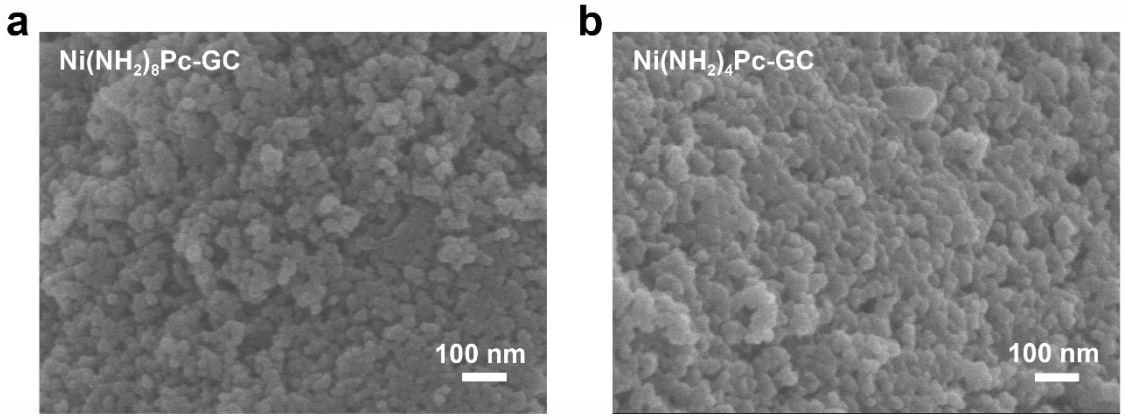


**Figure S18.** After constant potential electrolysis at -0.73 V *vs.* RHE for 10 hours, the SEM images of catalysts. (a) $Ni(NH_2)_8Pc$-GC. (b) $Ni(NH_2)_4Pc$-GC.

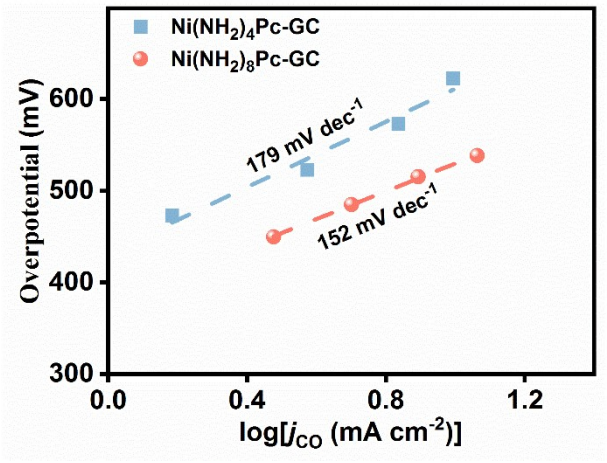


**Figure S19.** Tafel plots of $Ni(NH_2)_8Pc$-GC and $Ni(NH_2)_4Pc$-GC.

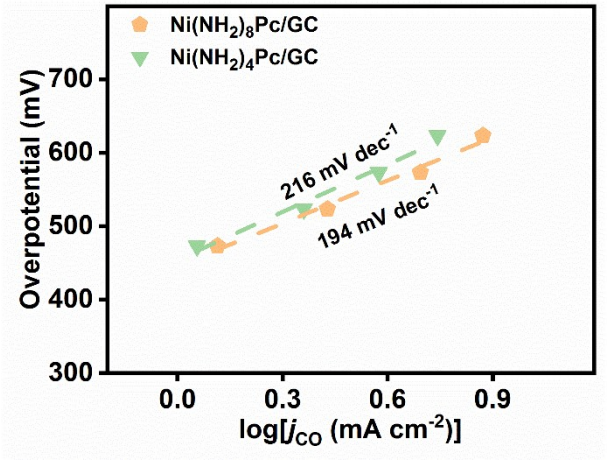


**Figure S20.** Tafel plots of $Ni(NH_2)_8Pc$/GC and $Ni(NH_2)_4Pc$/GC.

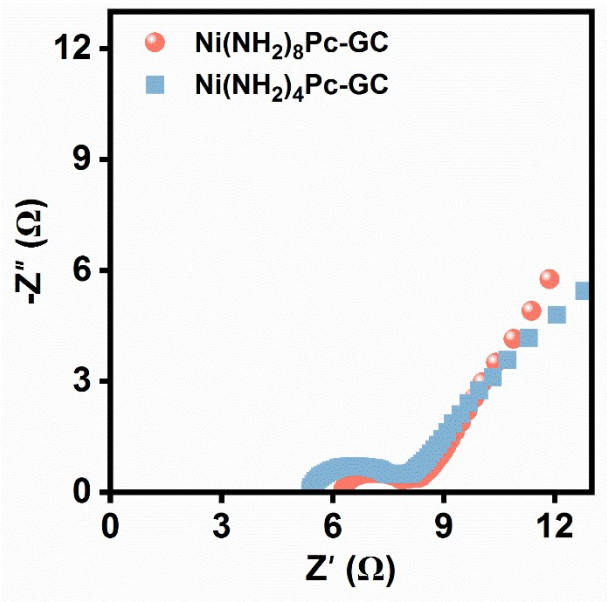


**Figure S21.** Nyquist plots of $Ni(NH_2)_8Pc$-GC and $Ni(NH_2)_4Pc$-GC.

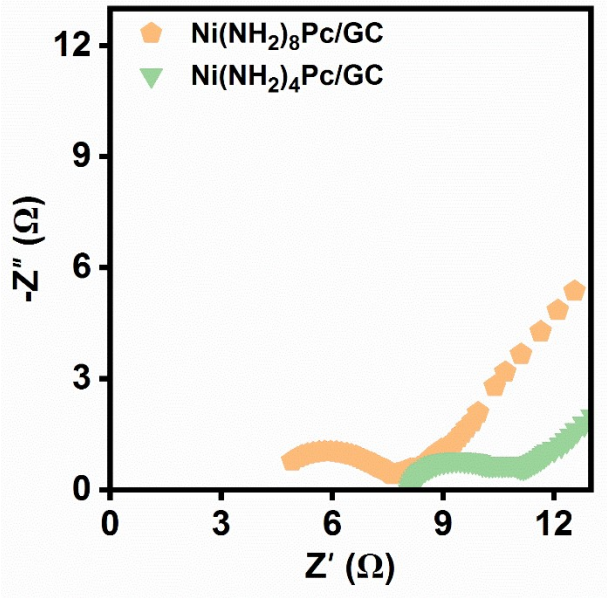


**Figure S22.** Nyquist plots of $Ni(NH_2)_8Pc$/GC and $Ni(NH_2)_4Pc$/GC.

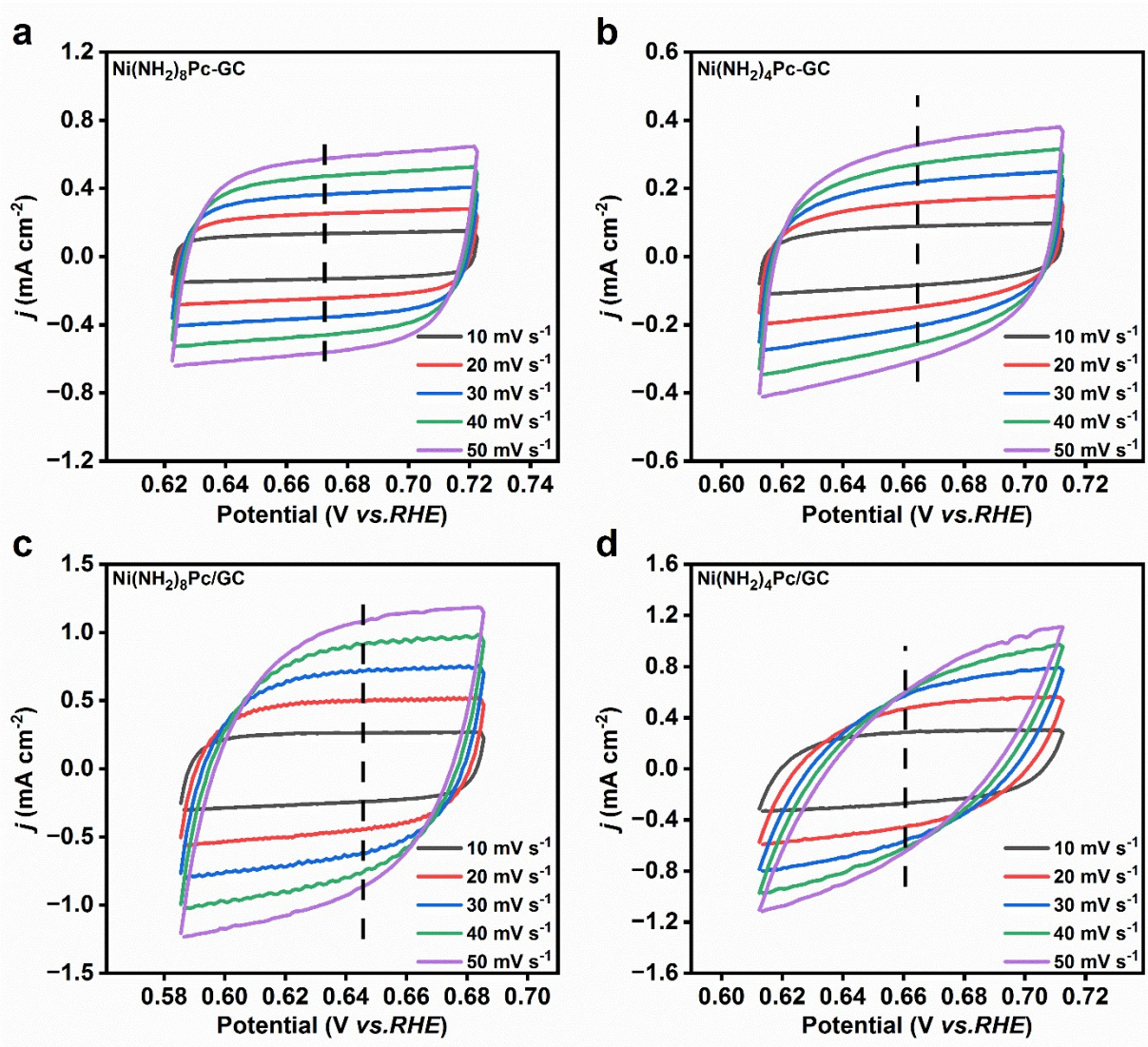


**Figure S23.** Electrochemical surface area measurements were performed in Ar-saturated 0.5 M $KHCO_3$. Current density of double-layer charging in cyclic voltammograms (CVs) at varied scan rates of catalysts. (a) $Ni(NH_2)_8Pc$-GC. (b) $Ni(NH_2)_4Pc$-GC. (c) $Ni(NH_2)_8Pc$/GC. (d) $Ni(NH_2)_4Pc$/GC.

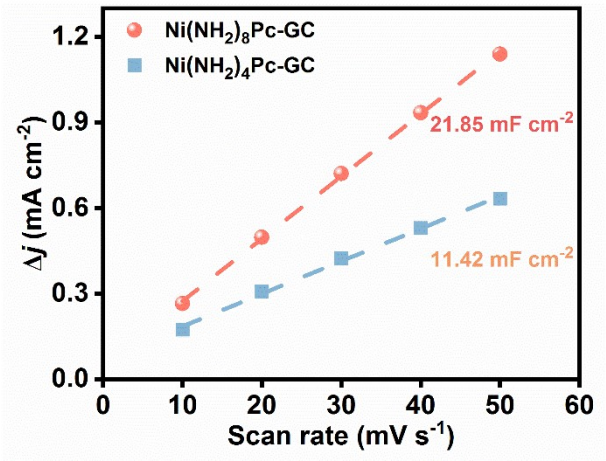


**Figure S24.** Capacitance values of $Ni(NH_2)_8Pc$-GC and $Ni(NH_2)_4Pc$-GC.

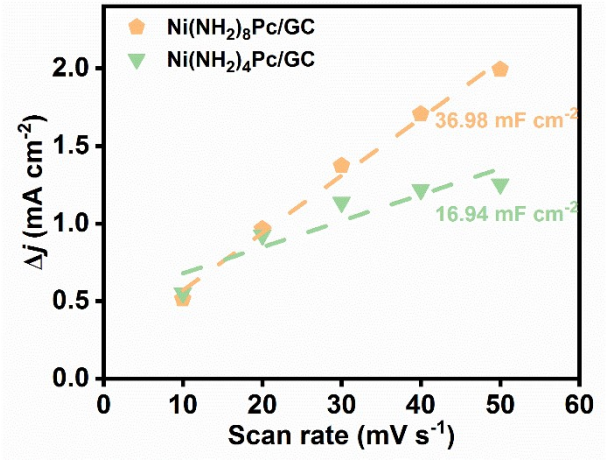


**Figure S25.** Capacitance values of $Ni(NH_2)_8Pc$/GC and $Ni(NH_2)_4Pc$/GC.

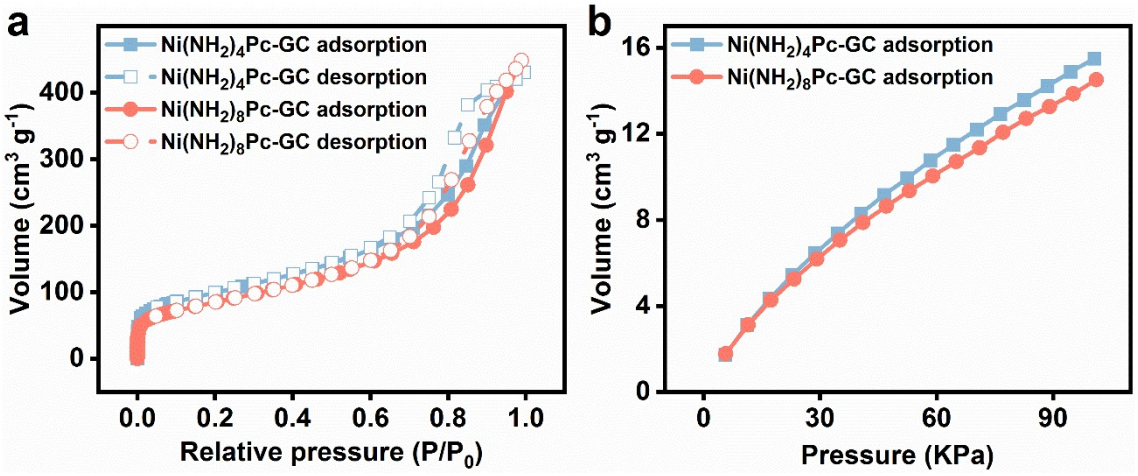


**Figure S26.** (a) $N_2$ adsorption-desorption isotherms at 77 K. (b) $CO_2$ adsorption isotherm at 298 K of $Ni(NH_2)_8Pc$-GC and $Ni(NH_2)_4Pc$-GC.

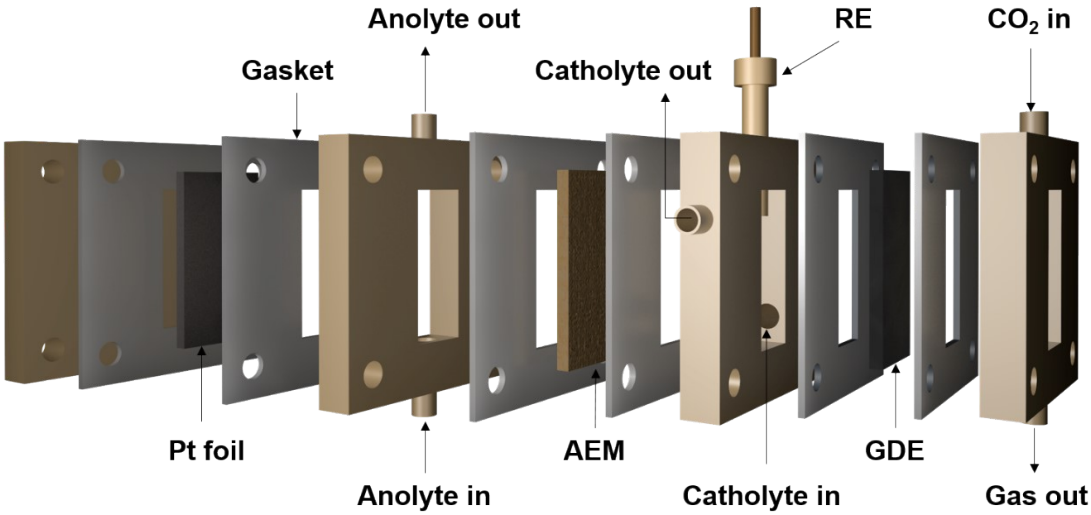


**Figure S27.** Schematic diagram of the reconstruction module of the flow cell.

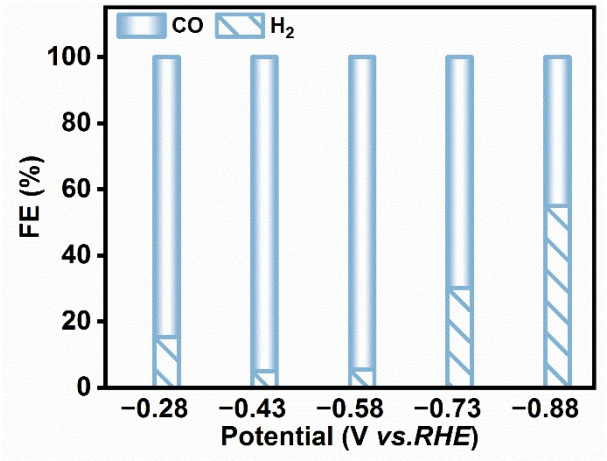


**Figure S28.** FEs of $Ni(NH_2)_4Pc$-GC in the flow cell with 1 M KOH as the electrolyte.

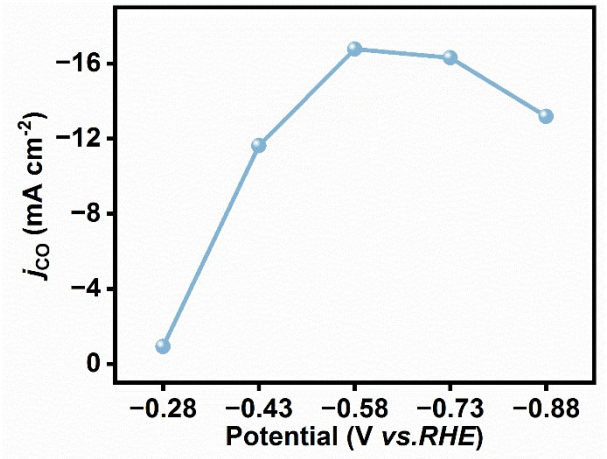


**Figure S29.** CO partial current density of $Ni(NH_2)_4Pc$-GC in the flow cell with 1 M KOH as the electrolyte.

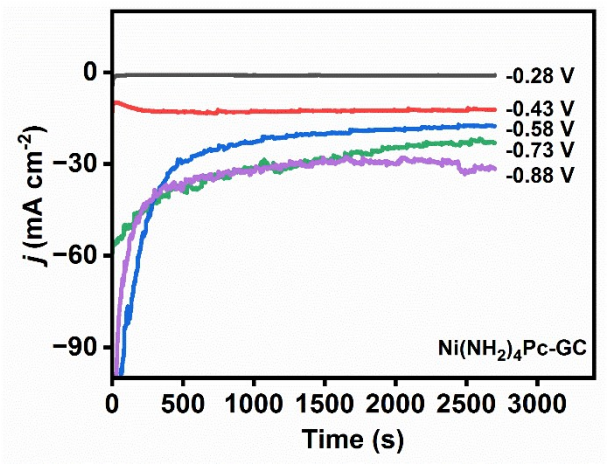


**Figure S30.** Total current densities of $Ni(NH_2)_4Pc$-GC at different applied potentials in the flow cell with 1 M KOH as the electrolyte.

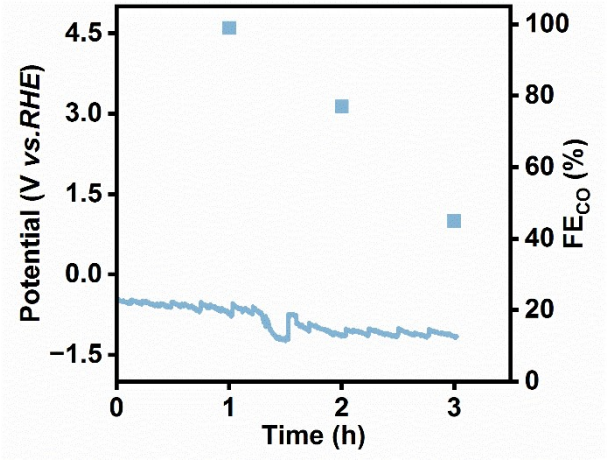


**Figure S31.** Long-term chronopotentiometric stability with a current density of 100 mA $cm^{-2}$ of $Ni(NH_2)_4Pc$-GC.

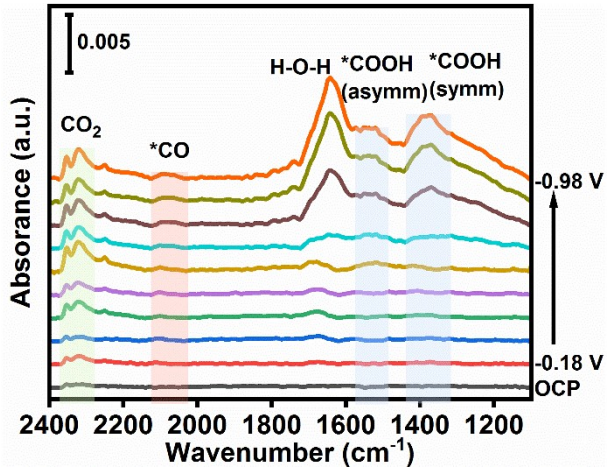


**Figure S32.** Potential-dependent ATR-SEIRAS spectra of $Ni(NH_2)_8Pc$-GC.

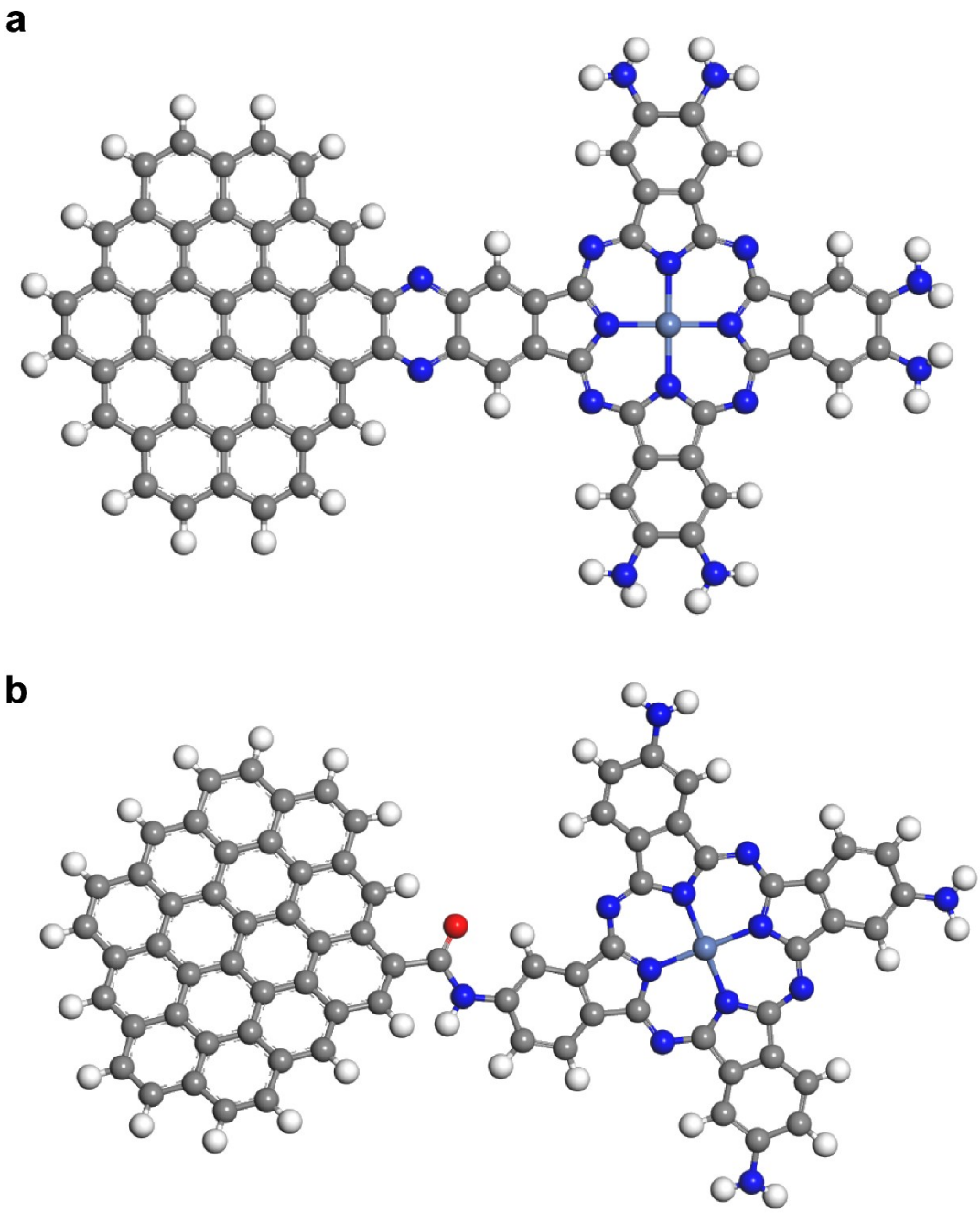


**Figure S33.** a) Model of $Ni(NH_2)_8Pc$-GC. b) Model of $Ni(NH_2)_4Pc$-GC. Color-code atoms represent Ni (lightseagreen), C (gray), N (blue), O (red) and H (white).

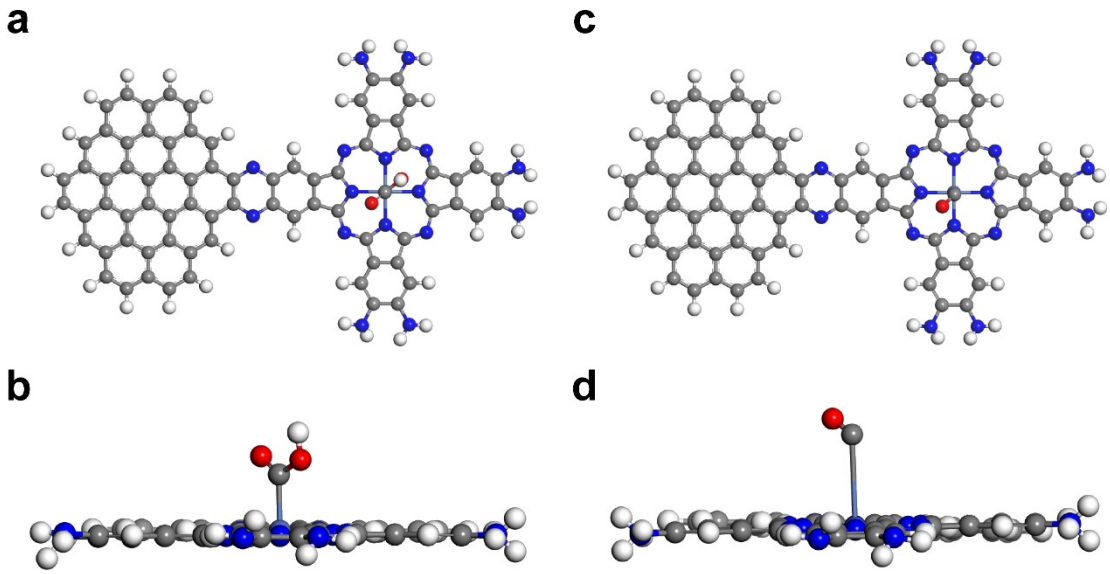


**Figure S34.** Adsorption configurations on $Ni(NH_2)_8Pc$-GC. (a-b) *COOH. (c-d) *CO. Color-code atoms represent Ni (lightseagreen), C (gray), N (blue), O (red) and H (white).

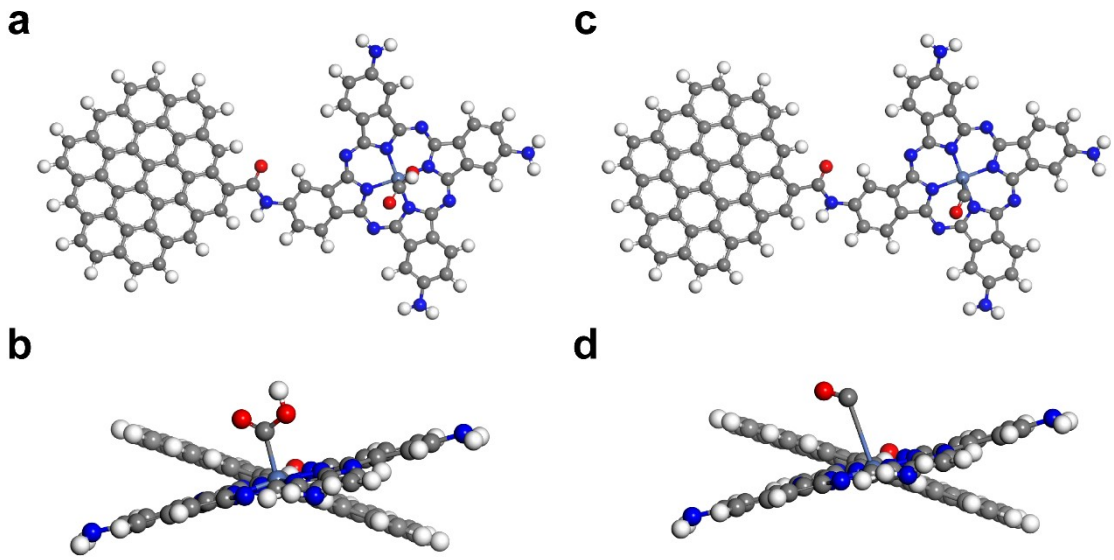


**Figure S35.** Adsorption configurations on $Ni(NH_2)_4Pc$-GC. (a-b) *COOH. (c-d) *CO. Color-code atoms represent Ni (lightseagreen), C (gray), N (blue), O (red) and H (white).

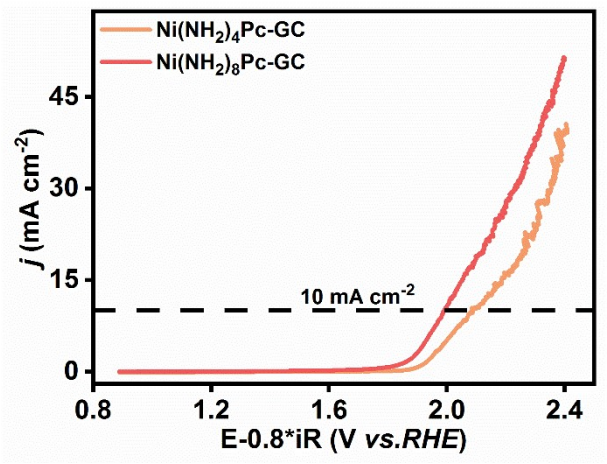


**Figure S36.** LSV curves in 0.8 M $KHCO_3$ solution at with scan rate of 5 mV $s^{-1}$ and 80% iR compensation of $Ni(NH_2)_8Pc$-GC and $Ni(NH_2)_4Pc$-GC.

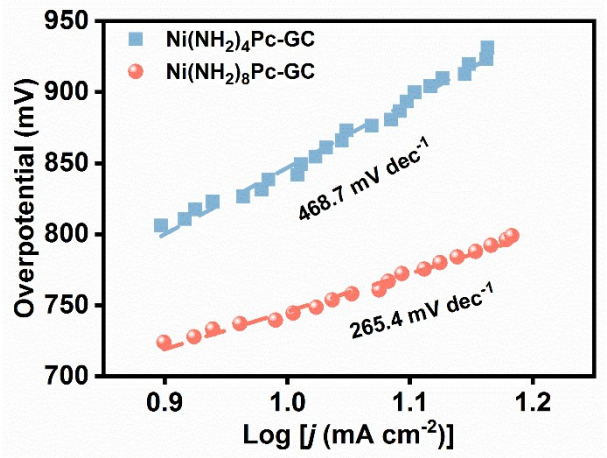


**Figure S37.** Tafel plots of $Ni(NH_2)_8Pc$-GC and $Ni(NH_2)_4Pc$-GC in 0.8 M $KHCO_3$ solution.

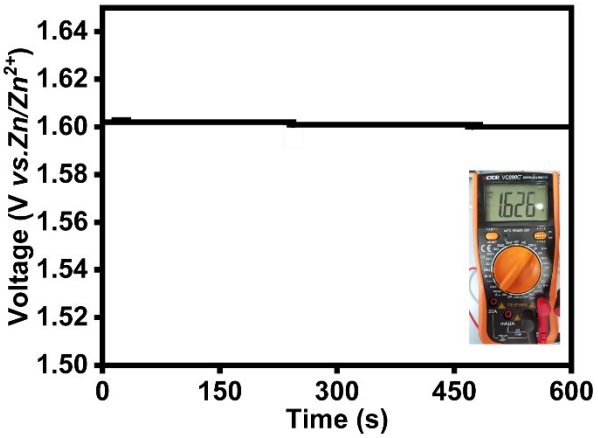


**Figure S38.** The open circuit voltage-time curve for the assembled Zn-$CO_2$ battery cell. Insert the photograph of the OCV measured by a multimeter.


**Figure S39.** Photographic image of two Zn-$CO_2$ batteries connected in series, which exhibit an OCV of 2.65 V measured by a multimeter.

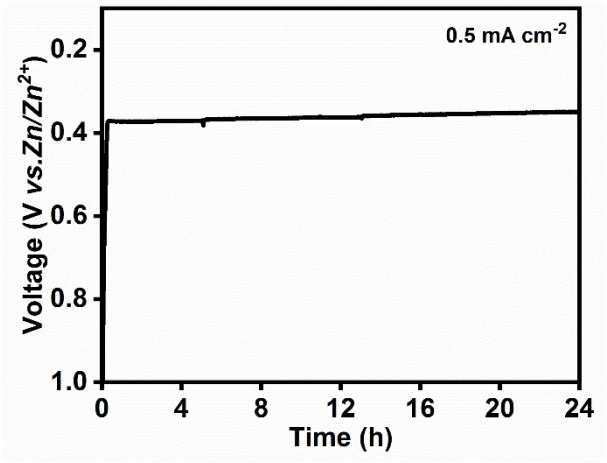


**Figure S40.** Prolonged discharge curve at -0.5 mA $cm^{-2}$ with $Ni(NH_2)_4$Pc-GC cathode in a Zn-$CO_2$ battery.

**Table S1.** Performances comparison of our catalysts with other recently reported representative nickel-based catalysts for $CO_2RR$ in H-type cell

| Catalysts | Potential (V) | $FE_{CO}$ (%) | $j_{CO}$ (mA $cm^{-2}$) | TOF ($h^{-1}$) | Reference |
|---|---|---|---|---|---|
| **$Ni(NH_2)_8Pc$-GC** | **-0.9** | **99.8** | **17.6** | **22, 618** | **This work** |
| **$Ni(NH_2)_4Pc$-GC** | **-0.9** | **91.4** | **15.2** | **7, 267** | |
| **$Ni(NH_2)_8Pc$/GC** | **-0.9** | **82.3** | **14.9** | **4, 277** | |
| **$Ni(NH_2)_4Pc$/GC** | **-0.9** | **63.3** | **7.8** | **2, 889** | |
| $Ni_2$-$N_4$-$C_2$ | -0.8 | 96.6 | 17.9 | 4, 606 (-1 V) | 1 |
| H-NiPc/CNT | -0.9 | ~ 90.0 | 17.5 | 13, 860 | 2 |
| NiPc/CNT | -0.9 | < 90.0 | 5.0 | 2, 960 | |
| NiPc-TFPN COF | -0.9 | 99.8 | 14.1 | 490 | 3 |
| PyNiPc/CNT （9.1 wt%） | -0.8 | ~ 100.0 | 20.0 | 8, 715 | 4 |
| | -0.9 | ~ 100.0 | ~ 30.0 | 12, 832 | |
| NiPc/CNT | -0.8 | 78.0 | < 3.0 | 1, 025 | 5 |
| NiPc | -0.8 | < 40.0 | 1.0 | < 10 | |
| NiPc-Cu-NH : CB (1 : 0.5) | -0.7 | 43.0 | 2.6 | 1, 404 | 6 |
| NiPc-$NiO_4$ | -1.2 | < 85.0 | 34.5 | 2, 603 | 7 |
| Ni-G | -0.8 | 82.6 | 16.9 | 6, 089 | 8 |
| Ni-CNT-20 | -0.8 | 98.8 | 9.1 | 2, 110 | |
| Ni-CNT-40 | -0.8 | 100.0 | 5.7 | 582.19 | |
| Ni@$C_3N_4$-CN | -1.2 | > 90.0 | 46.8 | 22, 000 | 9 |
| Ni@$C_3N_4$ | -1.2 | < 10.0 | 0.8 | 410 | |
| $NiN_4$-CB | -0.8 | < 98.7 | 5.0 | 1, 345 | 10 |

**Table S2.** Performances comparison of our catalysts with other recently reported representative nickel-based catalysts for $CO_2RR$ in GDE cell

| Catalysts | Potential (V) | $FE_{CO}$ (%) | $j_{CO}$ (mA $cm^{-2}$) | TOF ($h^{-1}$) | Reference |
|---|---|---|---|---|---|
| **$Ni(NH_2)_8Pc$-GC** | **-1.0** | **99.7** | **244.0** | **342, 295** | **This work** |
| **$Ni(NH_2)_4Pc$-GC** | **-0.9** | **45.1** | **31.2** | **14, 666** | |
| $(NHx)_{16}$-NiPc/CNTs | -1.2 | ~ 100.0 | ~ 250.0 | 60, 000 | 11 |
| Me-NiPc/CNTs | -1.2 | < 20.0 | ~ 20.0 | 5, 000 | |
| NiTAPc/CNT | -0.7 | 99.9 | 149.8 | 150, 840 (max) | 12 |
| | -0.8 | 94.6 | 473.0 | | |
| Ni-SAs-CNT | -0.4 | ~ 95.0 | 200.0 | 246, 000 | 13 |
| Ni-NG (MEA) | 2.8 (cell voltage) | > 90.0 | 200.0 | 210, 000 | 14 |
| C800NiA | -0.4 | 99.0 | > 300.0 | 41, 000 | 15 |
| Ni-NCB (MEA) | 2.7 (cell voltage) | 73.8 | 102.4 | 22, 896 | 16 |

**Table S3.** Performances comparison of our catalysts with other recently reported representative nickel-based catalysts for Zn-$CO_2$ batteries

| Catalysts | Maximum powder density (mW $cm^{-2}$) | Cycle current density (mA $cm^{-2}$) | Cycle time (h) | Reference |
|---|---|---|---|---|
| **$Ni(NH_2)_8Pc$-GC** | **0.7** | **0.5** | **50** | **This work** |
| **$Ni(NH_2)_4Pc$-GC** | **0.6** | **0.5** | **32** | |
| NiPG | 0.3 | 0.3 | 13 | 17 |
| CA/N-Ni | 0.5 | 0.5 | 30 | 18 |
| NiFe-DASC | 1.4 | 5.0 | 90 | 19 |
| Ni-$N_3$-C | 1.1 | 2.0 | - | 20 |
| Ni-$N_3$-NCNFs | 1.1 | 2.0 | 45 | 21 |

## References


1. X. Cao, L. Zhao, B. Wulan, D. Tan, Q. Chen, J. Ma and J. Zhang, Atomic Bridging Structure of Nickel–Nitrogen–Carbon for Highly Efficient Electrocatalytic Reduction of $CO_2$, *Angew. Chem. Int. Ed.*, 2021, **61**, e202113918.
2. Y. J. Sa, H. Jung, D. Shin, H. Y. Jeong, S. Ringe, H. Kim, Y. J. Hwang and S. H. Joo, Thermal Transformation of Molecular $Ni^{2+}$–$N_4$ Sites for Enhanced $CO_2$ Electroreduction Activity, *ACS Catal.*, 2020, **10**, 10920-10931.
3. M. Lu, M. Zhang, C. G. Liu, J. Liu, L. J. Shang, M. Wang, J. N. Chang, S. L. Li and Y. Q. Lan, Stable Dioxin-Linked Metallophthalocyanine Covalent Organic Frameworks (COFs) as Photo-Coupled Electrocatalysts for $CO_2$ Reduction, *Angew. Chem. Int. Ed.*, 2021, **60**, 4864-4871.
4. D.-D. Ma, S.-G. Han, C. Cao, X. Li, X.-T. Wu and Q.-L. Zhu, Remarkable electrocatalytic $CO_2$ reduction with ultrahigh $CO/H_2$ ratio over single-molecularly immobilized pyrrolidinonyl nickel phthalocyanine, *Appl. Catal. B Environ.*, 2020, **264**, 118530-118537.
5. Z. Zhang, J. Xiao, X. J. Chen, S. Yu, L. Yu, R. Si, Y. Wang, S. Wang, X. Meng, Y. Wang, Z. Q. Tian and D. Deng, Reaction Mechanisms of Well-Defined Metal-$N_4$ Sites in Electrocatalytic $CO_2$ Reduction, *Angew. Chem. Int. Ed.*, 2018, **57**, 16339-16342.
6. Z. Meng, J. Luo, W. Li and K. A. Mirica, Hierarchical Tuning of the Performance of Electrochemical Carbon Dioxide Reduction Using Conductive Two-Dimensional Metallophthalocyanine Based Metal–Organic Frameworks, *J. Am. Chem. Soc.*, 2020, **142**, 21656-21669.
7. J. D. Yi, D. H. Si, R. Xie, Q. Yin, M. D. Zhang, Q. Wu, G. L. Chai, Y. B. Huang and R. Cao, Conductive Two-Dimensional Phthalocyanine-based Metal–Organic Framework Nanosheets for Efficient Electroreduction of $CO_2$, *Angew. Chem. Int. Ed.*, 2021, **60**, 17108-17114.
8. C. Guo, S. Liu, Z. Chen, B. Li, L. Chen, C. V. Singh, B. Liu and Q. Mao, How does mass transfer influence electrochemical carbon dioxide reduction reaction? A case study of Ni molecular catalyst supported on carbon, *Chem. Commun.*, 2021, **57**, 1384-1387.
9. Q. Wang, K. Liu, K. Hu, C. Cai, H. Li, H. Li, M. Herran, Y.-R. Lu, T.-S. Chan, C. Ma, J. Fu, S. Zhang, Y. Liang, E. Cortés and M. Liu, Attenuating metal-substrate conjugation in atomically dispersed nickel catalysts for electroreduction of $CO_2$ to CO, *Nat. Commun.*, 2022, **13**, 6082.
10. C. Wang, H. Ren, Z. Wang, Q. Guan, Y. Liu and W. Li, A promising single-atom Co-N-C catalyst for efficient $CO_2$ electroreduction and high-current solar conversion of $CO_2$ to CO, *Appl. Catal. B Environ.*, 2022, **304**, 120958-120965.
11. S. G. Han, M. Zhang, Z. H. Fu, L. Zheng, D. D. Ma, X. T. Wu and Q. L. Zhu, Enzyme-Inspired Microenvironment Engineering of a Single-Molecular Heterojunction for Promoting Concerted Electrochemical $CO_2$ Reduction, *Adv. Mater.*, 2022, **34**, 2202830.
12. K. Chen, M. Cao, Y. Lin, J. Fu, H. Liao, Y. Zhou, H. Li, X. Qiu, J. Hu, X. Zheng, M. Shakouri, Q. Xiao, Y. Hu, J. Li, J. Liu, E. Cortés and M. Liu, Ligand Engineering in Nickel Phthalocyanine to Boost the Electrocatalytic Reduction of $CO_2$, *Adv. Funct. Mater.*, 2021, **32**, 2111322.
13. G. Hwa Jeong, Y. Chuan Tan, J. Tae Song, G.-Y. Lee, H. Jin Lee, J. Lim, H. Young Jeong, S. Won, J. Oh and S. Ouk Kim, Synthetic multiscale design of nanostructured Ni single atom catalyst for superior $CO_2$ electroreduction, *Chem. Eng. J.*, 2021, **426**, 131063.
14. K. Jiang, S. Siahrostami, T. Zheng, Y. Hu, S. Hwang, E. Stavitski, Y. Peng, J. Dynes, M.

Gangisetty, D. Su, K. Attenkofer and H. Wang, Isolated Ni single atoms in graphene nanosheets for high-performance $CO_2$ reduction, *Energy Environ. Sci.*, 2018, **11**, 893-903.
15. S. A. Abbas, J. T. Song, Y. C. Tan, K. M. Nam, J. Oh and K.-D. Jung, Synthesis of a Nickel Single-Atom Catalyst Based on $Ni–N_{4–x}C_x$ Active Sites for Highly Efficient $CO_2$ Reduction Utilizing a Gas Diffusion Electrode, *ACS Appl. Energy Mater.*, 2020, **3**, 8739-8745.
16. T. Zheng, K. Jiang, N. Ta, Y. Hu, J. Zeng, J. Liu and H. Wang, Large-Scale and Highly Selective $CO_2$ Electrocatalytic Reduction on Nickel Single-Atom Catalyst, *Joule*, 2019, **3**, 265-278.
17. R. Yang, J. Xie, Q. Liu, Y. Huang, J. Lv, M. A. Ghausi, X. Wang, Z. Peng, M. Wu and Y. Wang, A trifunctional Ni–N/P–O-codoped graphene electrocatalyst enables dual-model rechargeable $Zn–CO_2/Zn–O_2$ batteries, *Journal of Materials Chemistry A*, 2019, **7**, 2575-2580.
18. Y. Zhang, X. Wang, S. Zheng, B. Yang, Z. Li, J. Lu, Q. Zhang, N. M. Adli, L. Lei, G. Wu and Y. Hou, Hierarchical Cross-Linked Carbon Aerogels with Transition Metal-Nitrogen Sites for Highly Efficient Industrial-Level $CO_2$ Electroreduction, *Adv. Funct. Mater.*, 2021, **31**, 2104377.
19. Z. Zeng, L. Y. Gan, H. Bin Yang, X. Su, J. Gao, W. Liu, H. Matsumoto, J. Gong, J. Zhang, W. Cai, Z. Zhang, Y. Yan, B. Liu and P. Chen, Orbital coupling of hetero-diatomic nickel-iron site for bifunctional electrocatalysis of $CO_2$ reduction and oxygen evolution, *Nat. Commun.*, 2021, **12**, 4088.
20. Y. Zhang, L. Jiao, W. Yang, C. Xie and H. L. Jiang, Rational Fabrication of Low-Coordinate Single-Atom Ni Electrocatalysts by MOFs for Highly Selective $CO_2$ Reduction, *Angew. Chem. Int. Ed.*, 2021, **60**, 7607-7611.
21. W. Zheng, Y. Wang, L. Shuai, X. Wang, F. He, C. Lei, Z. Li, B. Yang, L. Lei, C. Yuan, M. Qiu, Y. Hou and X. Feng, Highly Boosted Reaction Kinetics in Carbon Dioxide Electroreduction by Surface-Introduced Electronegative Dopants, *Adv. Funct. Mater.*, 2021, **31**, 2008146.